



Publication Year	2018
Acceptance in OA@INAF	2020-11-13T15:11:18Z
Title	þ The extended He II » 4686 emission in the extremely n 052E seen with MUSE
Authors	Kehrig, C.; Vílchez, J. M.; Guerrero, M. A.; Iglesias-Páramo, J.; HUNT, Leslie Kipp; et al.
DOI	10.1093/mnras/sty1920
Handle	http://hdl.handle.net/20.500.12386/28331
Journal	MONTHLY NOTICES OF THE ROYAL ASTRONOMICAL SOCIETY
Number	480

The extended He II $\lambda 4686$ emission in the extremely metal-poor galaxy SBS 0335 – 052E seen with MUSE

C. Kehrig,¹ J. M. Vílchez,^{1*} M. A. Guerrero,¹ J. Iglesias-Páramo,^{1,2} L. K. Hunt,³ S. Duarte-Puertas¹ and G. Ramos-Larios⁴

¹*Instituto de Astrofísica de Andalucía, CSIC, Apartado de correos 3004, E-18080 Granada, Spain*

²*Estación Experimental de Zonas Áridas (CSIC), Ctra. de Sacramento s/n, La Caada, E-04120, Almería, Spain*

³*INAF – Osservatorio Astrofisico di Arcetri, Largo E. Fermi, 5, I-50125, Firenze, Italy*

⁴*Instituto de Astronomía y Meteorología, Dpto. de Física, CUCEI, Universidad de Guadalajara Av. Vallarta No. 2602, C.P. 44130, Guadalajara, Jalisco, Mexico*

Accepted 2018 July 12. Received 2018 July 11; in original form 2018 March 29

ABSTRACT

SBS 0335 – 052E, one of the most metal-poor ($Z \sim 3\text{--}4$ per cent Z_{\odot}) He II-emitter starbursts known in the nearby Universe, is studied using optical VLT/MUSE spectroscopic and *Chandra* X-ray observations. We spatially resolved the spectral map of the nebular He II $\lambda 4686$ emission from which we derived for the first time the total He II-ionizing energy budget of SBS 0335 – 052E. The nebular He II line is indicative of a quite hard ionizing spectrum with photon energies > 4 Ryd, and is observed to be more common at high- z than locally. Our study rules out a significant contribution from X-ray sources and shocks to the He II photoionization budget, indicating that the He⁺ excitation is mainly due to hot stellar continua. We discovered a new WR knot, but we also discard single Wolf–Rayet stars as the main responsible for the He II ionization. By comparing observations with current models, we found that the He II-ionization budget of SBS 0335 – 052E can only be produced by either single, rotating metal-free stars or a binary population with $Z \sim 10^{-5}$ and a ‘top-heavy’ initial mass function. This discrepancy between the metallicity of such stars and that of the H II regions in SBS 0335 – 052E is similar to results obtained by Kehrig et al. for the very metal-deficient He II-emitting galaxy IZw18. These results suggest that the He II ionization is still beyond the capabilities of state-of-the-art models. Extremely metal-poor, high-ionizing starbursts in the local Universe, like SBS 0335 – 052E, provide unique laboratories for exploring in detail the extreme conditions likely prevailing in the reionization era.

Key words: galaxies: dwarf – galaxies: individual: SBS 0335 – 052E – galaxies: ISM – galaxies: starburst – galaxies: stellar content.

1 INTRODUCTION

The cosmic dawn ($6 \lesssim z \lesssim 10$) marks a major phase transition of the Universe, during which the ‘first light’ [metal-free stars (or the so-called PopIII-stars) and the subsequent formation of numerous low-mass, extremely metal-poor galaxies] appeared, putting an end to the dark ages. The details of the reionization history reflect the nature of these first sources, which is currently completely unconstrained and the subject of considerable observational and theoretical efforts (e.g. Bromm 2013; Fialkov, Barkana & Visbal 2014; Visbal, Bryan & Haiman 2017). In recent years, *Hubble Space Telescope* (HST) deep field surveys (e.g. HUDF, CANDELS-deep) have improved

the statistics of galaxies at $z > 6$. Very soon, *James Webb Space Telescope* (JWST) will be studying the sources identified at this epoch. At $z \gtrsim 6$, however, observing the ultraviolet (UV) photons ($10 < \lambda < 130$ nm) gets progressively more difficult due to the increasing opacity of the intergalactic medium (IGM; e.g. Dijkstra, Mesinger & Wyithe 2011). Even JWST will be able to study in detail (i.e. spectroscopically) only the brightest sources ($M > 10^{10} M_{\odot}$; Windhorst et al. 2006), rather than the more common lower mass galaxies that are expected to reionize the Universe (e.g. Bouwens et al. 2015), for which only the integrated properties can be derived.

An immediately accessible approach is to identify galaxies at lower redshifts with properties similar to galaxies in the very early Universe. To do this, we need to distinguish the salient observational features that would be associated with such objects. He II emission (at $\lambda 1640$ and $\lambda 4686$ Å in the rest-frame UV and optical ranges,

* E-mail: jvm@iaa.es

respectively), observed to be more frequent in high- z galaxies than locally (e.g. Kehrig et al. 2011; Cassata et al. 2013), is indicative of far harder ionizing radiation than that seen in nearby systems, as photons with energy beyond 54.4 eV ($\equiv \lambda \leq 228 \text{ \AA}$) are required to twice ionize He. Star-forming (SF) galaxies with lower metal content tend to have larger narrow (nebular) He II line intensities compared to those with higher metallicities (e.g. Guseva, Izotov & Thuan 2000). This agrees with the expected harder spectral energy distribution (SED) at the lower metallicities typical in the distant Universe. Theoretical arguments suggest that PopIII-stars and nearly metal-free ($Z \lesssim Z_{\odot}/100$) stars have spectra hard enough to produce many He⁺-ionizing photons, and so the high-ionization He II line has been considered one of the best signatures to single out candidates for the elusive PopIII-hosting galaxies (e.g. Tumlinson & Shull 2000; Schaerer 2003; Visbal, Haiman & Bryan 2015). Although recent observations indicate that high-ionization emission appears to be more usual at the highest redshifts, the observational signatures of such ionization are not always unambiguous (e.g. Cassata et al. 2013; Gräfener & Vink 2015; Visbal, Haiman & Bryan 2016; Stark 2016; Mainali et al. 2017). Recently, Berg et al. (2018) detected high-ionization narrow emission lines (e.g. CIV1548,1550, He II1640, O III]1661,1666) in a metal-deficient lensed galaxy at $z \sim 2$. They found that the relative emission line strengths can be reproduced with a very high-ionization, low-metallicity starburst with binaries, with the exception of He II which requires an extra ionization source likely from extreme stellar populations.

The nebular He II line is the response of the galaxy gas to the He II-ionizing continuum ($\lambda \leq 228 \text{ \AA}$), and the hot, massive He II-ionizing stars, when not obscured, emit most of their radiation in the FUV ($\lambda \leq 2000 \text{ \AA}$). Based on current facilities, it is not possible to obtain direct extreme-UV observations of a such star at any redshift. As of today, individual stars cannot be safely resolved beyond the Local Group, and empirical constraints on massive stellar models are still limited to the SMC metallicity ($\sim 1/5 Z_{\odot}$; e.g. Kehrig et al. 2011; Herrero et al. 2012; Massey 2013; Garcia et al. 2014; Massey et al. 2014). Although significant progress has been made observationally and theoretically, modelling massive stellar evolution, in particular at the low metallicity regime, continues to be challenge (e.g. Puls, Vink & Najarro 2008; Tramper et al. 2011; Langer 2012; Muijres et al. 2012; Smith 2014; Szécsi et al. 2015; Georgy, Hirschi & Ekström 2016; Sander et al. 2017). Ultimately our understanding of metal-poor, hot massive stars remains elusive which propagates to a lack of understanding of the formation of high-ionization lines as He II. Therefore detailed studies on the origin of nebular He II at low redshifts are required to better interpret far-away narrow He II-emitters and hence gaining a deeper understanding of the reionization era. Low metallicity, He II-emitting local SF galaxies provide useful constraints on the little-known SEDs of metal-poor, hot massive stars and are unique laboratories in which to test stellar population synthesis models at sub-SMC metallicities (see e.g. Kehrig et al. 2008, 2013, 2015; Senchyna et al. 2017).

The goal of this paper is to seek a deeper understanding of the nebular He II emission in the nearby galaxy SBS 0335 – 052E. This study is based on Multi-Unit Spectroscopic Explorer (MUSE)/VLT optical integral field spectroscopy and *Chandra* X-ray observations (see Section 2). SBS 0335 – 052E, at a distance of 54 Mpc (NED¹), was discovered in the Second Byurakan Survey by Izotov et al. (1990). It presents an extremely low nebular oxygen abundance

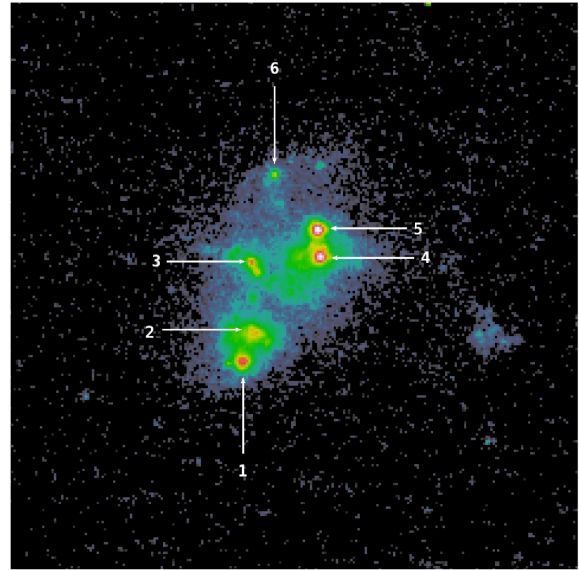


Figure 1. *HST* ACS/F220W archival image of SBS 0335-052E (*HST* Proposal ID 10575; PI: G.Östlin). The brightest SSCs as identified by Thuan et al. (1997) are labelled. The image is $6 \times 6 \text{ arcsec}^2$. North is up and east is to the left-hand side.

of $12+\log(\text{O}/\text{H}) \sim 7.2\text{--}7.3$ ($\sim 3\text{--}4$ per cent Z_{\odot} ²; e.g. Izotov et al. 1990; Melnick, Heydari-Malayeri & Leisy 1992; Izotov et al. 1999; Papaderos et al. 2006), placing it among the most metal-poor SF galaxies with nebular He II emission known in the local Universe. The hard extreme-UV ionizing photons and the very low metallicity gas present in SBS 0335 – 052E are features prevailing in the early Universe, which makes this galaxy an excellent low-redshift analog.

SBS 0335 – 052E undergoes a vigorous starburst and hosts extremely massive young clusters (see Johnson, Hunt & Reines 2009, and references therein). All star formation occurs in six very blue and compact ($< 60 \text{ pc}$) super-star clusters (SSCs) with a mean age of $\sim 6 \text{ Myrs}$ (see Thuan, Izotov & Lipovetsky 1997; Reines, Johnson & Hunt 2008). In Fig. 1, we show the *HST*/ACS UV image of SBS 0335 – 052E. In this image, we can see the six brightest SSCs of the galaxy which are found distributed over a region of $\sim 2 \text{ arcsec}$ ($\sim 520 \text{ pc}$ at the distance of 54 Mpc).

The paper is organized as follows: Section 2 details the observations and data reduction; Section 3 describes flux measurements and optical emission line intensity maps, while Section 4 details the spatially resolved He II $\lambda 4686$ -emitting region. The discussion on the origin of the nebular He II $\lambda 4686$ emission and comparison of models with observations are covered in Section 5. Finally, Section 6 summarizes the main conclusions derived from this work.

2 OBSERVATIONS

2.1 Optical integral field spectroscopic data

The MUSE (Bacon et al. 2014) data of SBS 0335 – 052E were obtained in 2015 November 16th and 17th under the ESO program ID 096.B-0690A (PI: M.Hayes). The observations were carried out in the wide field mode which provides a field of view (FoV) of $1 \times 1 \text{ arcmin}^2$ with a sampling of $0.2 \times 0.2 \text{ arcsec}^2$ in the wavelength range $\sim 4600\text{--}9366 \text{ \AA}$.

¹NASA/IPAC Extragalactic Database.

²Assuming a solar metallicity $12+\log(\text{O}/\text{H})_{\odot}=8.69$ (Asplund et al. 2009).

We have retrieved the fully reduced data cubes of SBS 0335 – 052E from the ESO archive. The reduction of the raw data used version 1.6.1 of the MUSE Instrument Pipeline with default parameters, which consists of the standard procedures of bias subtraction, flat fielding, sky subtraction, wavelength calibration, and flux calibration. The cube analysed here is the result of eight exposures of 2840 s each, and the data were taken at airmasses ~ 1.0 . The spectral resolving power is $R = \lambda/\delta\lambda = 2988$. The point spread function (PSF) full width at half-maximum (FWHM) ranges from ~ 0.6 to 0.7 arcsec. We note that these data have already been independently analysed by Herenz et al. (2017).

2.2 X-ray observations

SBS 0335 – 052E was observed with the front-illuminated CCD array ACIS-I onboard the *Chandra X-Ray Observatory* on 2000 September 7 for a total exposure time of 47.6 ks (Observation ID: 796; PI: Thuan). Observations were carried out in the Very Faint mode. We retrieved level 1 and level 2 processed data from the *Chandra* Data Center, but actually only the level 1 data were used after reprocessing them with the *chandra_repro* tool of the CHANDRA X-RAY CENTER SOFTWARE CIAO v4.9 using CALDB 4.7.3. The data reduction included standard removal of pixel randomization, cleaning of ACIS background for the Very Faint mode, and bad pixels masking.

The event list was further filtered to select good *ASCA* grades. The data were affected by a few episodes of relatively high background (above the nominal ACIS-I background rate $\simeq 0.20$ cts, s $^{-1}$ chip $^{-1}$ in the energy range 0.5–7.0 keV) that were excised for further data analysis. The net exposure time was then reduced to 32.5 ks. The data analysis was performed using HEASARC FTOOLS and XSPEC v12.9.1 routines (Arnaud 1996). The astrometry of the X-ray data was refined using X-ray sources in the FoV spatially coincident with optical sources in the *HST* archival WFPC2 *F791W* image.

3 OPTICAL FLUX MEASUREMENTS AND EMISSION LINE MAPS

We derived the emission-line fluxes from the $\sim 90\,000$ spaxels³ of the MUSE data cube following the steps described next. First, we fit the continuum level adjacent to every emission line for each spaxel spectrum. This procedure was repeated several times by varying the local continuum position. The final continuum level and its associated uncertainty (or continuum noise) for each line were adopted to be the average and standard deviation of the repeated measurements, assuming these follow a normal distribution. After subtracting the final continuum level from every line, we derive the line flux by fitting a Gaussian profile to each emission line using the IDL-based routine MPFIT (Markwardt 2009); the peak intensity, the line width σ and the central wavelength λ_c for each line are kept as free parameters. In the case of the $H\alpha$ + [N II] lines, we fit the three lines simultaneously keeping the same line width and radial velocity for [N II] and $H\alpha$, and a nitrogen [N II] $\lambda 6584$ /[N II] $\lambda 6548$ line ratio of 3.

Using our own IDL scripts, we combine the line fluxes with the position of the fibres on the sky to create the maps of emission lines presented in this paper. Fig. 2 displays the He II $\lambda 4686$, [O I]

$\lambda 6300$, [N II] $\lambda 6584$, $H\beta$, [O III] $\lambda 5007$, and [S II] $\lambda 6717$ + 6731 emission line maps. As a guide to the reader, isocontours of the He II $\lambda 4686$ emission line flux are shown in all maps. The intensity distribution of $H\beta$ and [O III] $\lambda 5007$ are more extended than that of He II $\lambda 4686$, [O I] $\lambda 6300$, [N II] $\lambda 6584$, and [S II] $\lambda 6717$ + 6731 because those lines are among the brightest optical emission lines in the SBS 0335 – 052E spectra. The maps show wisps and/or filaments that surround the central strong emission region depicting the complex morphology of the ionized gas in SBS 0335 – 052E (see also Herenz et al. 2017).

4 THE SPATIALLY RESOLVED HE II $\lambda 4686$ -EMITTING REGION

The presence of narrow He II $\lambda 4686$ emission in SBS 0335 – 052E has been reported before. For instance, Melnick et al. (1992), Izotov et al. (1997), and Thuan & Izotov (2005) based on long-slit spectroscopy, show the narrow He II $\lambda 4686$ line in the spectrum of SBS 0335 – 052E. Izotov et al. (2006) first produced a He II $\lambda 4686$ spectral map of SBS 0335 – 052E using the VLT/GIRAFFE spectrograph. However, the superior spatial resolution of MUSE provides much more detailed emission-line flux maps, and therefore allows us to perform a broader study on the origin of the He II ionization in SBS 0335 – 052E, a subject still under debate not only for this galaxy but for other several local He II-emitting SF systems (e.g. Garnett et al. 1991; Izotov et al. 2006; Kehrig et al. 2011; Shirazi & Brinchmann 2012; Kehrig et al. 2013, 2015). We will discuss this point further in Section 5.

Figs 2 and 3 reveal a highly extended He II $\lambda 4686$ -emitting region from our IFS data (see also Herenz et al. 2017). The spatial distribution of He II is quite different from that of the other emission lines (see Fig. 2) The He II emission consists of a roundish oval shape component with a diameter of ~ 5 arcsec (~ 1.3 kpc at the distance of 54 Mpc) over the galaxy core, and a shell-like structure (called here ‘He II shell’) which are connected to each other. The He II-emitting zone extends out to distances $\gtrsim 6$ arcsec (~ 1.5 kpc) from the youngest SSCs (SSCs #1 and #2; see e.g. Reines et al. 2008), and presents three peaks spatially displaced from the brightest stellar clusters (see top right-hand panel from Fig. 3).

From our data, we checked that the FWHM of the He II $\lambda 4686$ line is comparable to that of the other nebular emission lines (e.g. $H\beta$, [O III] $\lambda 5007$). The measured values of the mean (μ) and standard deviation (σ) for the FWHM(He II)/FWHM($H\beta$) and FWHM(He II)/FWHM([O III] $\lambda 5007$) ratios are $\mu = 1.13$ ($\sigma = 0.09$) and $\mu = 1.10$ ($\sigma = 0.10$), respectively. The narrow line profile for the He II $\lambda 4686$ emission and its spatial extent is evidence of its nebular nature.

Based on the spatial distribution of the emission in He II, we created the 1D spectra for several regions by summing the flux in the spaxels within each of the corresponding areas displayed in Fig. 3. The spectra of the knots centered on the three peaks seen in the He II line map are named He II Knots A, B, and C; the area of their aperture extraction is 0.36 arcsec² each. The ‘He II shell’ integrated zone covers ~ 9.7 arcsec². We have also obtained the 1D spectrum for which we term He II main body (‘He II-MB’) by adding all He II-emitting spaxels with He II signal to noise ratio (S/N) > 10 ; thus exclusively the emission of the brighter He II ionized gas has been integrated in the He II MB spectrum. Finally, we obtained for the first time the integrated spectrum of SBS 0335 – 052E. To do so, we have integrated the flux in all the spaxels for which $H\alpha$ S/N (per spaxel) > 10 ; this corresponds to an area of ~ 340 arcsec²

³Individual elements of IFUs are often called ‘spatial pixels’ (commonly shortened to ‘spaxel’); the term is used to differentiate between a spatial element on the IFU and a pixel on the detector.

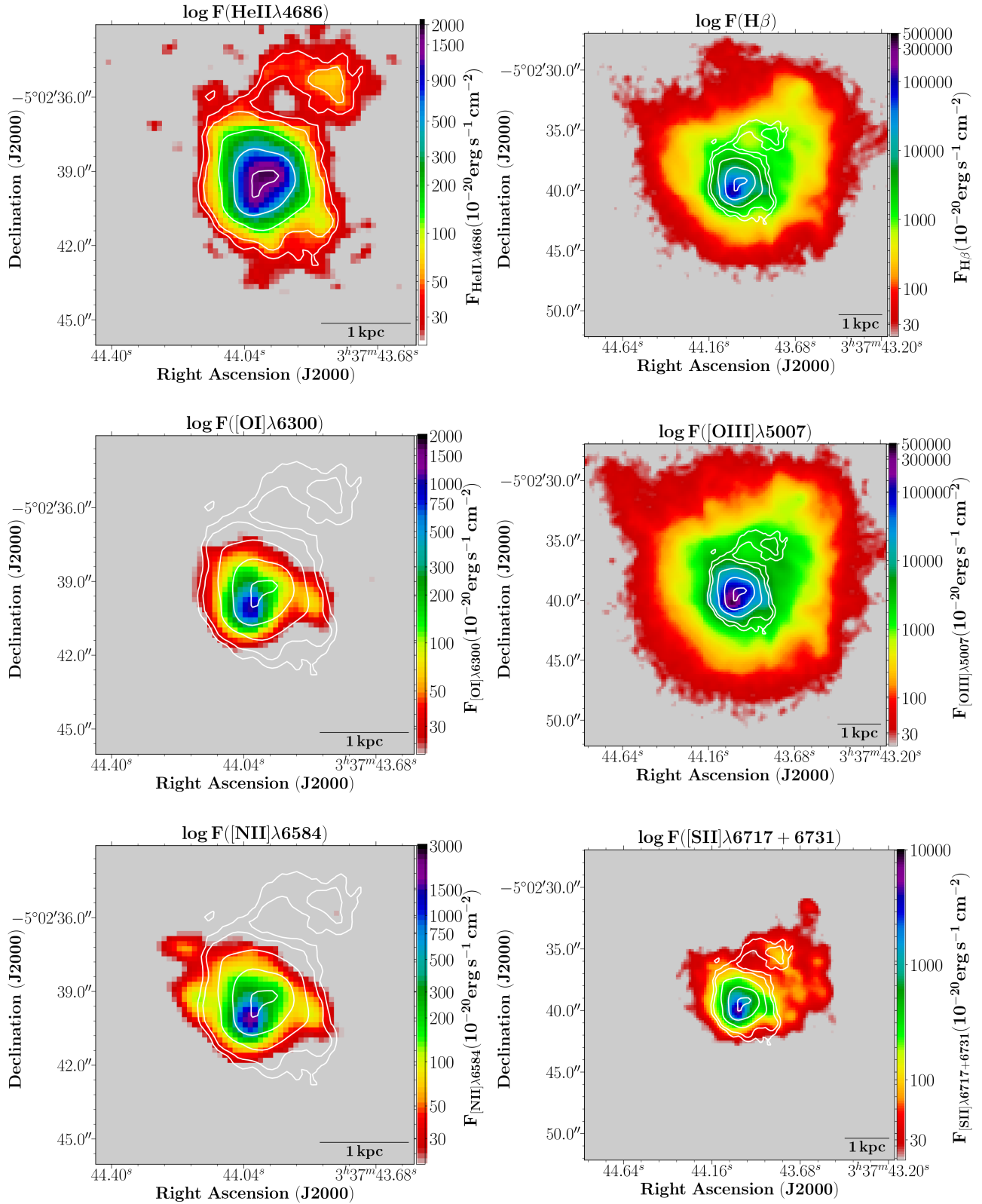


Figure 2. Emission line flux maps of SBS 0335 – 052E: He II $\lambda 4686$, [O I] $\lambda 6300$, [N II] $\lambda 6584$, H β , [O III] $\lambda 5007$, [S II] $\lambda 6717 + 6731$. For display purposes, all maps have been smoothed with a $\sigma=1$ pixel (0.2 arcsec) Gaussian Kernel, and are presented in logarithmic scale. Isocontours of the He II $\lambda 4686$ emission line flux are shown overplotted for reference. The maps for the weakest lines (left-hand column) show a smaller FoV in comparison to the brightest ones (right-hand column) for better visualization. North is up and east to the left.

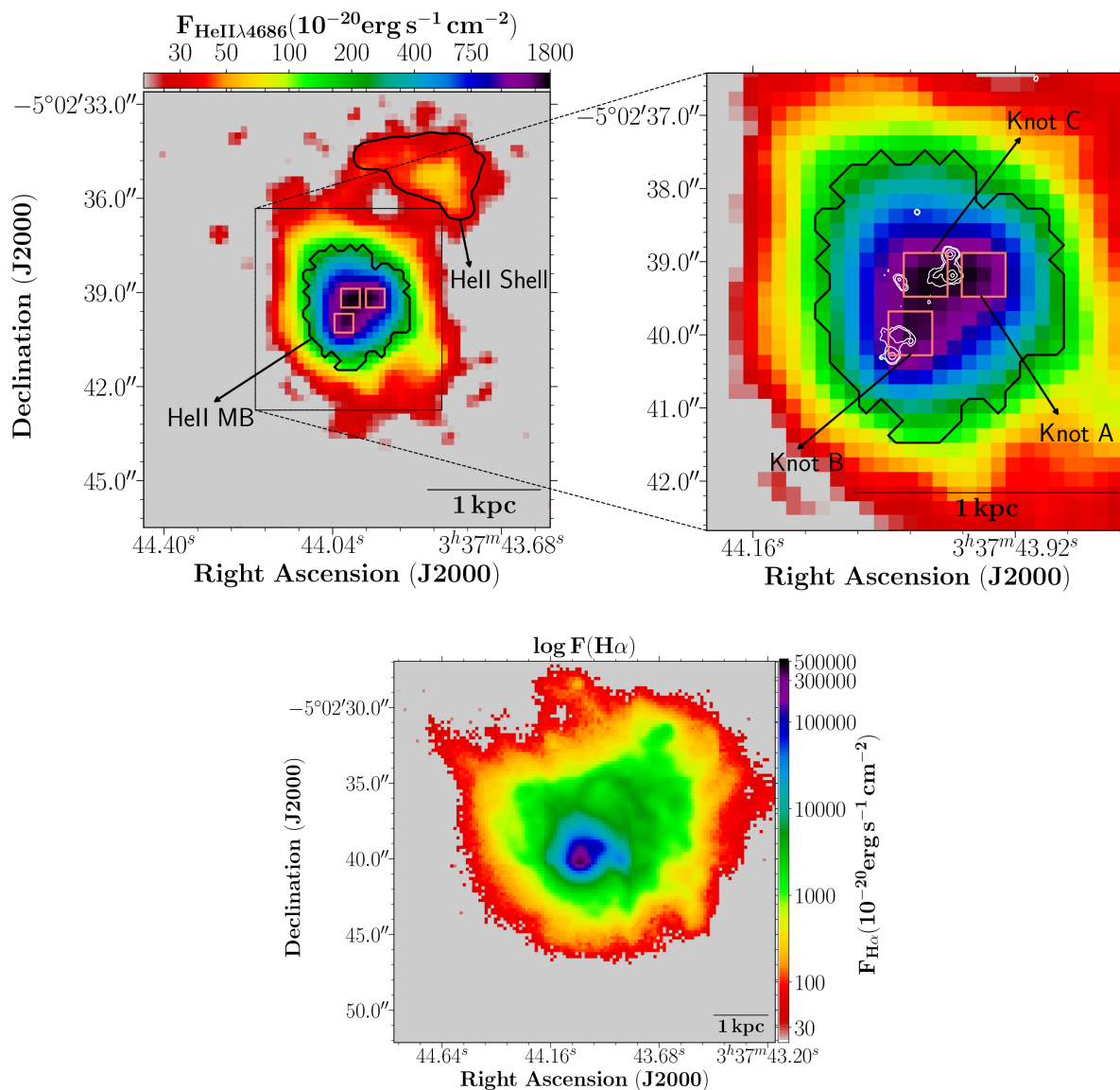


Figure 3. Top row: the He II $\lambda 4686$ map in two different scales showing the boundaries of the areas that we use to create the integrated spectra of the He II-emitting regions: He II shell, He II main body, and He II knots A,B,C (see the text and Table 1 for details); in the top right-hand panel the white lines mark the location of the brightest SSCs of SBS 0335-052E (see Fig. 1). Bottom row: the $\text{H}\alpha$ map showing the spaxels only with $\text{H}\alpha$ S/N (per pixel) > 10 . North is up and east to the left-hand side.

($\sim 23 \text{ kpc}^2$), enclosing basically all the nebular emission across our MUSE FOV (see the $\text{H}\alpha$ map in Fig. 3).

Fig. 4 presents the 1D spectra for the aforementioned regions of SBS 0335 – 052E. We measured the emission line fluxes of the 1D spectra with the SPLOT routine in IRAF⁴ by integrating all the line flux between two points given by the position of a local continuum. The continuum level is estimated by visually placing the graphics cursor at both sides of each line. This process was repeated several times for each emission line by varying the continuum position. We take the mean and the standard deviation of the repeated measurements as the final flux of each line and its asso-

ciated uncertainty, respectively. The reddening coefficient, $c(\text{H}\beta)$, corresponding to each summed spectra was computed from the ratio of the measured-to-theoretical $\text{H}\alpha/\text{H}\beta$ assuming the reddening law of Cardelli, Clayton & Mathis (1989), and case B recombination with electron temperature $T_e = 2 \times 10^4 \text{ K}$ and electron density $n_e = 100 \text{ cm}^{-3}$ (e.g. Papaderos et al. 2006) which give an intrinsic value of $\text{H}\alpha/\text{H}\beta = 2.75$ (Osterbrock & Ferland 2006). Reddening-corrected line intensities, normalized to $\text{H}\beta$, along with physical properties obtained from the 1D spectra are shown in Table 1.

The He II ionizing photon flux, $Q(\text{He II})$, can be derived from the reddening-corrected $L_{\text{He II } \lambda 4686}$, using the relation $Q(\text{He II}) = L_{\text{He II } \lambda 4686} / [j(\lambda 4686) / \alpha_B(\text{He II})]$ (Osterbrock & Ferland 2006). Making use of the integrated spectrum, and assuming case B recombination and an electron temperature $T_e = 2 \times 10^4 \text{ K}$ (e.g. Izotov et al. 2006; Papaderos et al. 2006), we computed for the first time the total He II ionizing photon flux,

⁴IRAF is distributed by the National Optical Astronomical Observatories, which are operated by the Association of Universities for Research in Astronomy, Inc., under cooperative agreement with the National Science Foundation.

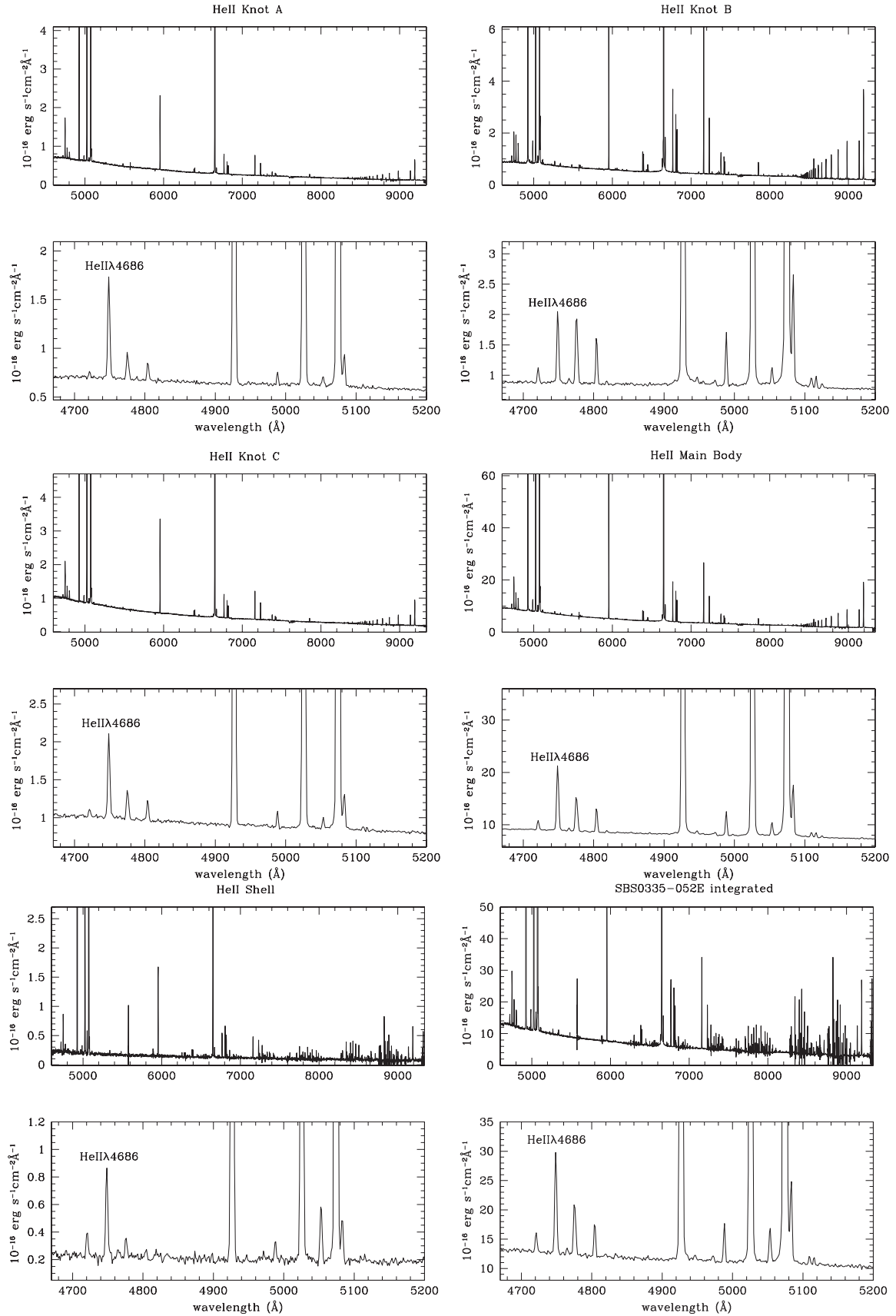


Figure 4. Flux-calibrated 1D spectra of the selected He II-emitting regions and the integrated spectrum of SBS 0335 – 052E (see the text for details). A zoom-in of the wavelength range $\sim 4670\text{--}5200\text{ \AA}$ is also displayed. The spectra are in units of $10^{-16}\text{ erg s}^{-1}\text{ \AA cm}^{-2}\text{ \AA}^{-1}$.

Table 1. De-reddened emission line-fluxes relative to 1000-I(H β) and physical properties from selected regions.

Wavelength	He II Knot A	He II Knot B	He II knot C	He II 'shell'	He II-MB ^a	Integrated ^b
4658 [Fe III]	2.4 \pm 0.4	2.60 \pm 0.10	3.5 \pm 0.4	10.5 \pm 0.5	3.40 \pm 0.11	4.47 \pm 0.26
4686 He II	60.8 \pm 0.6	14.20 \pm 0.10	46.0 \pm 0.7	39 \pm 1	27.14 \pm 0.13	26.08 \pm 0.32
4714 [Ar IV]+He I	16.3 \pm 0.5	16.10 \pm 0.20	16.8 \pm 0.5	7 \pm 1	16.49 \pm 0.11	14.93 \pm 0.29
4740 [Ar IV]	9.54 \pm 0.36	8.70 \pm 0.10	9.8 \pm 0.5	–	8.99 \pm 0.10	7.79 \pm 0.18
4861 H β	1000 \pm 1	1000 \pm 4	1000 \pm 1	1000 \pm 1	1000 \pm 1	1000 \pm 4
4959 [O III]	1052 \pm 1	1099 \pm 3	1171 \pm 1	774 \pm 1	1094 \pm 1	1006 \pm 4
5007 [O III]	3128 \pm 2	3231 \pm 9	3487 \pm 2	2336 \pm 2	3271 \pm 2	3002 \pm 8
5876 He I	87.29 \pm 0.20	128.95 \pm 0.38	93.99 \pm 0.28	89 \pm 1	105.75 \pm 0.25	101.34 \pm 0.33
6300 [O I]	3.70 \pm 0.20	8.78 \pm 0.06	5.15 \pm 0.12	7.5 \pm 0.4	7.17 \pm 0.04	8.04 \pm 0.15
6312 [S III]	5.20 \pm 0.20	7.23 \pm 0.06	5.60 \pm 0.13	7.3 \pm 0.4	6.36 \pm 0.05	6.09 \pm 0.23
6563 H α	2750 \pm 3	2665 \pm 9	2750 \pm 7	2750 \pm 3	2750 \pm 13	2750 \pm 10
6584 [N II]	4.90 \pm 0.30	12.00 \pm 0.30	5.90 \pm 0.26	10 \pm 1	9.30 \pm 0.04	10 \pm 1
6678 He I	22.50 \pm 0.10	33.70 \pm 0.10	23.36 \pm 0.21	24 \pm 1	27.02 \pm 0.11	26.10 \pm 0.15
6717 [S II]	13.50 \pm 0.10	23.30 \pm 0.10	16.43 \pm 0.11	28.66 \pm 0.38	20.48 \pm 0.11	22.79 \pm 0.39
6731 [S II]	11.20 \pm 0.10	19.80 \pm 0.10	13.02 \pm 0.13	22.2 \pm 0.4	17.0 \pm 0.5	17.1 \pm 0.6
c(H β)	0.22	0.00	0.20	0.13	0.10	0.10
-EW(H α) (Å)	656	1319	600	1400	1081	1030
-EW(H β) (Å)	97	300	96	305	187	199
F(H α) ^c	2.85 \times 10 ⁻¹⁴	6.98 \times 10 ⁻¹⁴	3.76 \times 10 ⁻¹⁴	2.20 \times 10 ⁻¹⁴	5.42 \times 10 ⁻¹³	7.95 \times 10 ⁻¹³
F(H β) ^c	1.03 \times 10 ⁻¹⁴	2.62 \times 10 ⁻¹⁴	1.37 \times 10 ⁻¹⁴	8.02 \times 10 ⁻¹⁵	1.97 \times 10 ⁻¹³	2.89 \times 10 ⁻¹³
F(He II) ^c	6.29 \times 10 ⁻¹⁶	3.73 \times 10 ⁻¹⁶	6.30 \times 10 ⁻¹⁶	3.14 \times 10 ⁻¹⁶	5.35 \times 10 ⁻¹⁵	7.54 \times 10 ⁻¹⁵
L(H β)(erg s ⁻¹)	3.61 \times 10 ³⁹	9.13 \times 10 ³⁹	4.77 \times 10 ³⁹	2.04 \times 10 ³⁹	6.88 \times 10 ⁴⁰	1.01 \times 10 ⁴¹
L(He II)(erg s ⁻¹)	2.19 \times 10 ³⁸	1.30 \times 10 ³⁸	2.20 \times 10 ³⁸	8.94 \times 10 ³⁷	1.87 \times 10 ³⁹	2.63 \times 10 ³⁹
Q(He II)(photon s ⁻¹) ^d	2.64 \times 10 ⁵⁰	1.56 \times 10 ⁵⁰	2.65 \times 10 ⁵⁰	1.32 \times 10 ⁵⁰	2.25 \times 10 ⁵¹	3.17 \times 10 ⁵¹
Q(H)(photon s ⁻¹) ^e	1.38 \times 10 ⁵²	3.39 \times 10 ⁵²	1.83 \times 10 ⁵²	1.07 \times 10 ⁵²	2.63 \times 10 ⁵³	3.86 \times 10 ⁵³
log ([O I]6300/H α)	-2.88	-2.48	-2.73	-2.57	-2.59	-2.53
log ([N II]6584/H α)	-2.74	-2.35	-2.67	-2.43	-2.47	-2.44
log ([S II]6717+31/H α)	-2.05	-1.79	-1.97	-1.73	-1.86	-1.84
log ([O III]5007/H β)	0.49	0.51	0.54	0.37	0.51	0.48
n _e ([S II])(cm ⁻³)	264	318	168	121	267	6

Notes. ^a'He II main body' (He II-MB) spectrum obtained by summing all He II-emitting spaxels with He II S/N > 10.

^bSBS 0335-052E integrated spectrum created by adding all spaxels with H α S/N > 10.

^cH β , H α and He II extinction-corrected fluxes in units of erg s⁻¹ cm⁻².

^dNumber of ionizing photons shortward of the He⁺ edge.

^eNumber of ionizing photons shortward of the H⁰ edge.

Q(He II)_{int} = 3.17 \times 10⁵¹ photons s⁻¹, in SBS 0335 – 052E. Q(He II)_{int} is a relevant quantity in order to study the origin of the nebular He II emission (see Kehrig et al. 2015, and see also Section 5). Using the same methodology, we also computed Q(He II) for the other selected regions of SBS 0335 – 052E mentioned above (see Table 1). From Table 1, we can see that the He II main body and the He II shell, together, produce a total of $\sim 2.38 \times 10^{51}$ He⁺-ionizing photons s⁻¹ which represents ~ 75 per cent of the integrated Q(He II)_{int}. This indicates that the contribution to the Q(He II)_{int} from the most external and faint He II emission from the SBS 0335 – 052E core is not negligible (~ 25 per cent). This highlights the importance of high-spatial resolution IFS for our analysis, which have allowed us to collect all He II emission free from aperture effect corrections required in single-fiber or long-slit spectroscopic observations.

5 ON THE ORIGIN OF THE HE II $\lambda 4686$ EMISSION AND IONIZING SOURCES

Despite numerous attempts to explain the origin of nebular He II emission in nearby and distant SF systems, there are many cases that are currently inconclusive (e.g. Guseva et al. 2000; Kehrig et al. 2011; Cassata et al. 2013; Gräfener & Vink 2015; Kehrig et al. 2015; Senchyna et al. 2017). The most popular scenarios for producing nebular He II emission involve X-ray sources, shocks,

and hot stellar ionizing continua (e.g. Garnett et al. 1991; Dopita & Sutherland 1996; Cerviño, Mas-Hesse & Kunth 2002; Schaerer 2003; Thuan & Izotov 2005; Shirazi & Brinchmann 2012; Kehrig et al. 2015). In the following, we discuss each of these possible He II ionizing sources in SBS 0335 – 052E.

5.1 X-ray emission

A preliminary inspection of the *Chandra* observations of SBS 0335 – 052E confirms the detection of faint X-ray emission as reported by Thuan et al. (2004). To investigate the correspondence between the spatial distribution of the X-ray, UV, and optical emissions in SBS 0335 – 052E, we made adaptively smoothed X-ray images in soft (0.6–1.4 keV) and hard (1.4–5.0 keV) bands with spatial resolution from 1.2 arcsec for bright point sources up to 1.8 arcsec for weak diffuse emission. These X-ray images are compared to the *HST* ACS/F220W and He II images in Fig. 5.

The comparison between the X-ray emission and the UV image reveals a source of hard X-ray emission (red contours in Fig. 5, left-hand panel) spatially coincident with the brightest SSCs at the core of SBS 0335 – 052E. At the spatial resolution of the X-ray images, the source is basically unresolved, but for a slight elongation along the south-east–north-west direction. Thuan et al. (2004) associated this source with SSC #2, although some additional emission was associated with SSCs #3, #4, and #5 (the SSCs are labelled in Fig. 1).

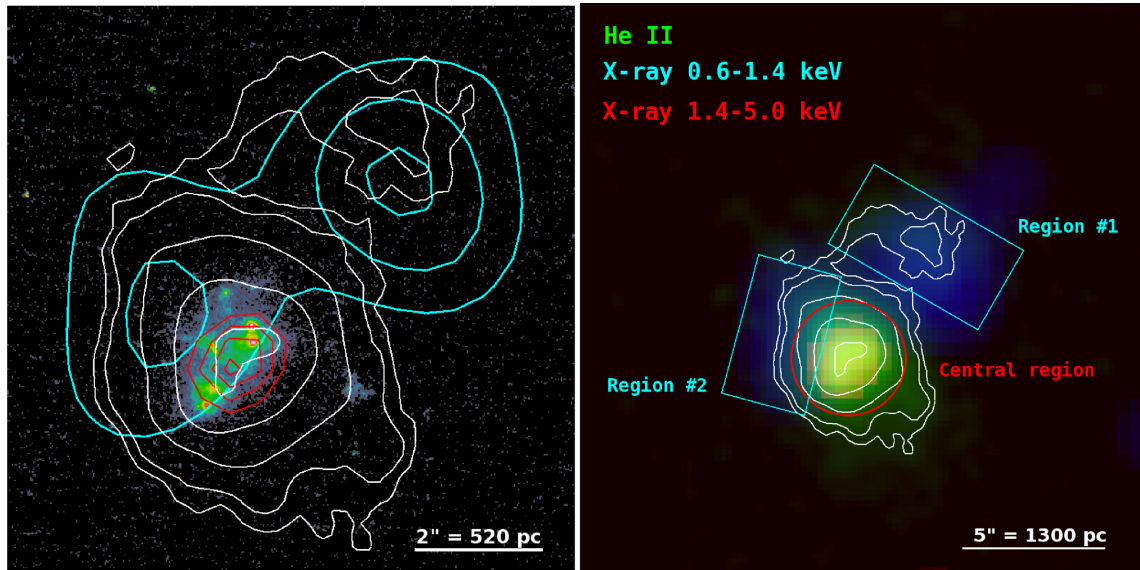


Figure 5. Left-hand panel: soft (cyan lines) and hard (red lines) X-ray contours overlaid on the *HST* ACS/F220W image of SBS 0335 – 052E. Right-hand panel: colour composite image of SBS 0335 – 052E in three bandpasses (blue=soft X-rays, red=hard X-rays, green=He II $\lambda 4686$ flux image). In both panels, the white curves represent the isocontours of the He II $\lambda 4686$ emission line flux. North is up and east is to the left-hand side.

Our analysis cannot provide a definitive association between this X-ray source and any of the SSCs; although at lower resolution, we can see that its peak is indeed closer to SSC #2 (see red contours in Fig. 5 left-hand panel). However, the distribution of the soft X-ray emission is utterly different from that of the hard X-ray emission, with one faint blob of diffuse emission towards the Northeast of the core of SBS 0335 – 052E and another one brighter towards the Northwest (cyan contours in Fig. 5, left-hand panel). The comparison of the soft X-ray and He II images reveals that the latter source of soft X-ray emission is confined by the He II Northwest shell (see Fig. 5, left- and right-hand panels).

According to the X-ray images presented above, we have extracted X-ray spectra from the apertures labeled ‘central region’, ‘region #1’, and ‘region #2’, as shown in Fig. 5, right-hand panel, corresponding to the central hard point source, and to the north-west and north-east sources of soft diffuse emission, respectively. The count numbers of these spectra are too low to allow detailed spectral fits. Indeed, the spectral analysis of the X-ray emission from the hard source presented by Thuan et al. (2004) could constrain neither the emission model (power-law or optically-thin plasma), nor its parameters. Assuming a hydrogen column density $N_{\text{H}} = 1 \times 10^{22} \text{ cm}^{-2}$, consistent with that used by Thuan et al. (2004), and a metallicity 3 per cent Z_{\odot} (e.g. Izotov et al. 1999, 2006; Papaderos et al. 2006), we find that the emission in this hard source is consistent with an optically-thin plasma emission model with a temperature of 3 keV. For comparison, Thuan et al. (2004) suggested plasma temperatures ~ 3 keV, and certainly in excess of 1.2 keV. As for the diffuse X-ray emission, the same metallicity of 3 per cent Z_{\odot} was assumed, but the hydrogen column density was reduced to $N_{\text{H}} = 5 \times 10^{20} \text{ cm}^{-2}$ to be consistent with the optical extinction $c(\text{H}\beta) = 0.13$ derived for ‘region #1’ and ‘region #2’ from the MUSE data. With these assumptions, the (even fainter) X-ray spectrum of the diffuse X-ray emission is found to be consistent with an optically thin plasma emission model at a temperature of 1 keV.

The intrinsic X-ray luminosities of the central hard point-like source and the north-west soft diffuse emission in the 0.3–5.0 keV band are 4×10^{39} and $3 \times 10^{38} \text{ erg s}^{-1}$, respectively. These X-ray

models (spectral shapes, luminosities, absorptions) have been convolved with the energy-dependent cross section of He^+ to estimate the effective X-ray ionizing power. We find $\log Q(\text{He II})$ to be 36.2 for the central hard source and 35.4 for the Northwest source confined within the He II shell. Clearly, these numbers show that the X-ray emission from the different sources found in SBS 0335 – 052E cannot provide the ionizing flux responsible for its He II emission (see Table 1). Moreover, the different models to describe the X-ray emission from SBS 0335 – 052E (for instance, a power-law) also result in similarly low values of $\log Q(\text{He II})$ that are well below the required value to ionize He II at the level observed in this galaxy.

5.2 A 2D view of the gas excitation from MUSE

The contributions of different ionization mechanisms to the line emission across a galaxy can be probed quantitatively using diagnostic line ratios (e.g. Baldwin, Phillips & Terlevich [BPT] 1981; Veilleux & Osterbrock 1987; Kewley et al. 2015). The three panels of Fig. 6 show the spatially resolved $[\text{N II}] \lambda 6584/\text{H}\alpha$, $[\text{S II}] \lambda \lambda 6717, 6731/\text{H}\alpha$, and $[\text{O I}] \lambda 6300/\text{H}\alpha$ versus $[\text{O III}] \lambda 5007/\text{H}\beta$ diagrams for SBS 0335 – 052E, while Fig. 7 displays the maps for such line ratios. These line ratios are not corrected for reddening, but their reddening dependence is negligible since they are calculated from lines which are close in wavelength. These optical diagnostic diagrams are commonly used to separate gas excitation dominated by massive star photoionization from other ionizing sources, including active galactic nucleus (AGNs), post-asymptotic giant branch stars and shocks (e.g. Kewley et al. 2001, 2006; Kehrig et al. 2012; Gomes et al. 2016; Davies et al. 2017). In Fig. 6, each circle represents the line ratios calculated from the emission line fluxes of an individual spaxel, where the red circles indicate the He II-emitting spaxels. The line ratios obtained from the one-dimensional (1D) spectra of selected regions across our FoV (see Section 4 and Table 1) are overplotted on the diagrams as triangles. The solid black curves on the three plots define the Kewley et al. (2001) theoretical upper bound to pure star formation. The dashed black curve on the $[\text{N II}] \lambda 6584/\text{H}\alpha$ -diagram traces the Kauffmann et al. (2003) empir-

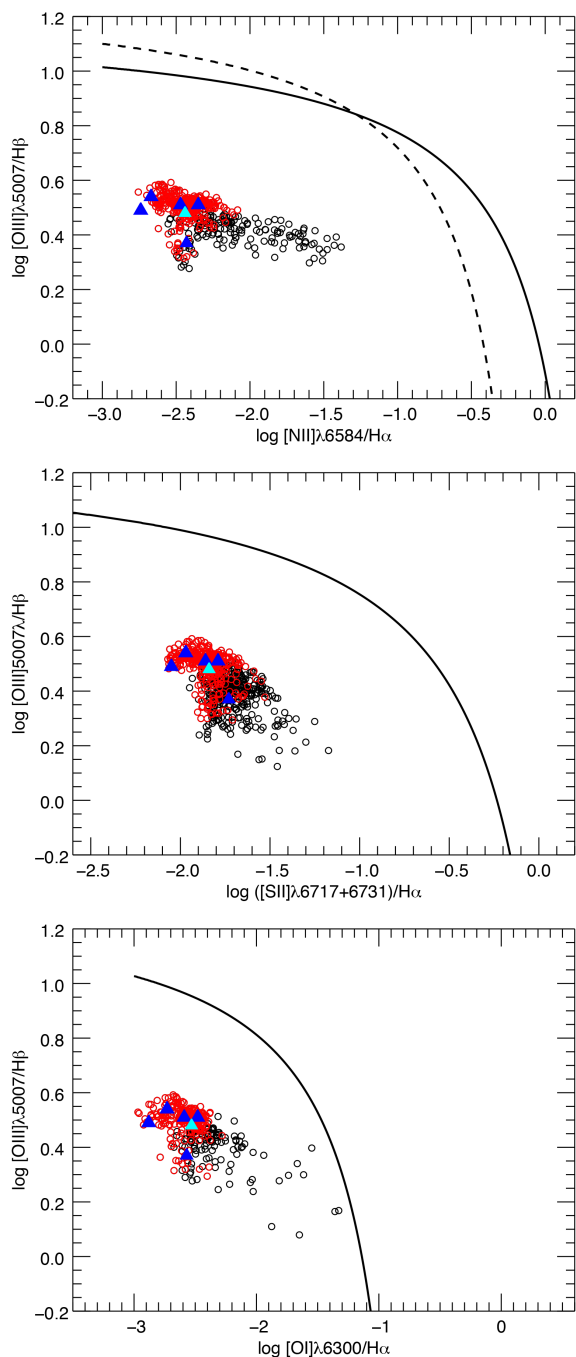


Figure 6. BPT diagnostic diagrams for SBS 0335 – 052E. From top to bottom: $\log ([\text{O III}] \lambda 5007/\text{H}\beta)$ versus $\log ([\text{N II}] \lambda 6584/\text{H}\alpha)$, $\log ([\text{O III}] \lambda 5007/\text{H}\beta)$ versus $\log ([\text{S II}] \lambda 6731,6717/\text{H}\alpha)$, and $\log ([\text{O III}] \lambda 5007/\text{H}\beta)$ versus $\log ([\text{O I}] \lambda 6300/\text{H}\alpha)$. Only fluxes with $\text{S/N} \geq 5$ are shown. Open circles correspond to individual spaxels from the data cube; red circles mark the individual He II-emitting spaxels. Overlaid as triangles are the line ratios measured from the 1D spectra of selected galaxy regions; the cyan triangle corresponds to the total integrated spectrum of SBS 0335 – 052E (see Section 4 and Table 1 for details on the 1D spectra). Overplotted as a black solid curve (in all three panels) is the theoretical maximum starburst model from Kewley et al. (2001), devised to isolate objects whose emission line ratios can be accounted for by the photoionization by massive stars (below and to the left-hand side of the curve) from those where some other source of ionization is required. The black-dashed curve in the [N II]/H α diagram represents the demarcation between SF galaxies (below and to the left-hand side of the curve) and AGNs defined by Kauffmann et al. (2003).

ical classification line, which marks out the upper boundary of the Sloan Digital Sky Survey star formation sequence. All spectra lying below these curves are dominated by star formation. As indicated in Fig. 6, for all positions in SBS 0335 – 052E our emission-line ratios fall in the general locus of SF objects according to the spectral classification scheme proposed by Kewley et al. (2001) and Kauffmann et al. (2003). Accordingly, photoionization from hot massive stars seems to be the dominant excitation mechanism within SBS 0335 – 052E, regardless of the locus in the galaxy.

Of course, in starburst systems, supernovae remnants (SNRs) and massive star winds might be present and produce shock-heated gas. The extension and complex morphology of the ionized gas in SBS 0335 – 052E indeed suggest that the gas excitation and hard ionization may be partially due to shocks. However, besides the BPT diagram results, our spatially resolved observations give other reasons why shocks are unlikely to be the main source of He⁺-ionizing photons in SBS 0335 – 052E. We find no sign of significant [S II]/H α and/or [O I] $\lambda 6300/\text{H}\alpha$ enhancement (a frequent indication of shock-excited gas; e.g. Skillman 1985; Dopita & Sutherland 1996; Allen et al. 2008) associated with the He II-emitting region (see Fig. 7). In particular, there is no [O I] $\lambda 6300$ emission with $\text{S/N} \geq 5$ at the location of the He II shell whose filamentary structure could, in principle, suggest an important shock excitation (see Fig. 2); the He II shell also shows low values of [S II]/H α associated with (see Fig. 7). Our measured values of [S II] $\lambda \lambda 6717,6731/\text{H}\alpha$ ratio ($\lesssim 0.03$) in the He II-emitting spaxels (see Fig. 6) are lower than the ones observed in SNRs ([S II] $\lambda \lambda 6717,6731/\text{H}\alpha \sim 0.5\text{--}1.0$; e.g. Smith et al. 1993) which points against He II shock ionization as well. Moreover, the characteristic [O III] temperature ($\sim 20\,000$ K; e.g. Izotov et al. 2006; Papaderos et al. 2006) in SBS 0335 – 052E is not as high as seen in classical SNRs (e.g. Blair, Kirshner & Chevalier 1981). These observational facts reinforce that notion that the formation of nebular He II in SBS 0335 – 052E is mainly due to stellar sources, as mentioned previously. Next, we explore the hot massive star scenario.

5.3 Hot stars ionizing continua

5.3.1 Models on a star-by-star basis

For many years, hot Wolf–Rayet stars (WRs) have been proposed to be a reasonable explanation for He II excitation, given the good correlation between the presence of narrow He II $\lambda 4686$ emission and WR features in SF systems mostly with metallicities $12+\log(\text{O}/\text{H}) \gtrsim 8$ (e.g. Schaerer 1996; Schaerer & Vacca 1998; Brinchmann, Kunth & Durret 2008). However, this correlation does not hold in all cases (e.g. Hadfield & Crowther 2007; Kehrig et al. 2011; Neugent & Massey 2011). Various studies have shown that nebular He II $\lambda 4686$ emission does not appear to be always associated with WRs, especially in metal-deficient objects (e.g. Guseva et al. 2000; Thuan & Izotov 2005; Shirazi & Brinchmann 2012). In principle, one could envisage that the lack of WR features in the spectrum of metal-poor galaxies with nebular He II $\lambda 4686$ emission is likely because of the reduced WR line luminosities expected at low metallicities (e.g. Crowther & Hadfield 2006). Of course, this interpretation might be valid in some cases, but not at all times; there are examples showing that the non-detection of WR signatures in some metal-deficient He II $\lambda 4686$ -emitting regions is not an effect of the weakness of WR bumps, confirming so the lack of connection of He II $\lambda 4686$ emission with the hard radiation from WRs (see Kehrig et al. 2008, 2013; Shirazi & Brinchmann 2012; Kehrig et al. 2015).

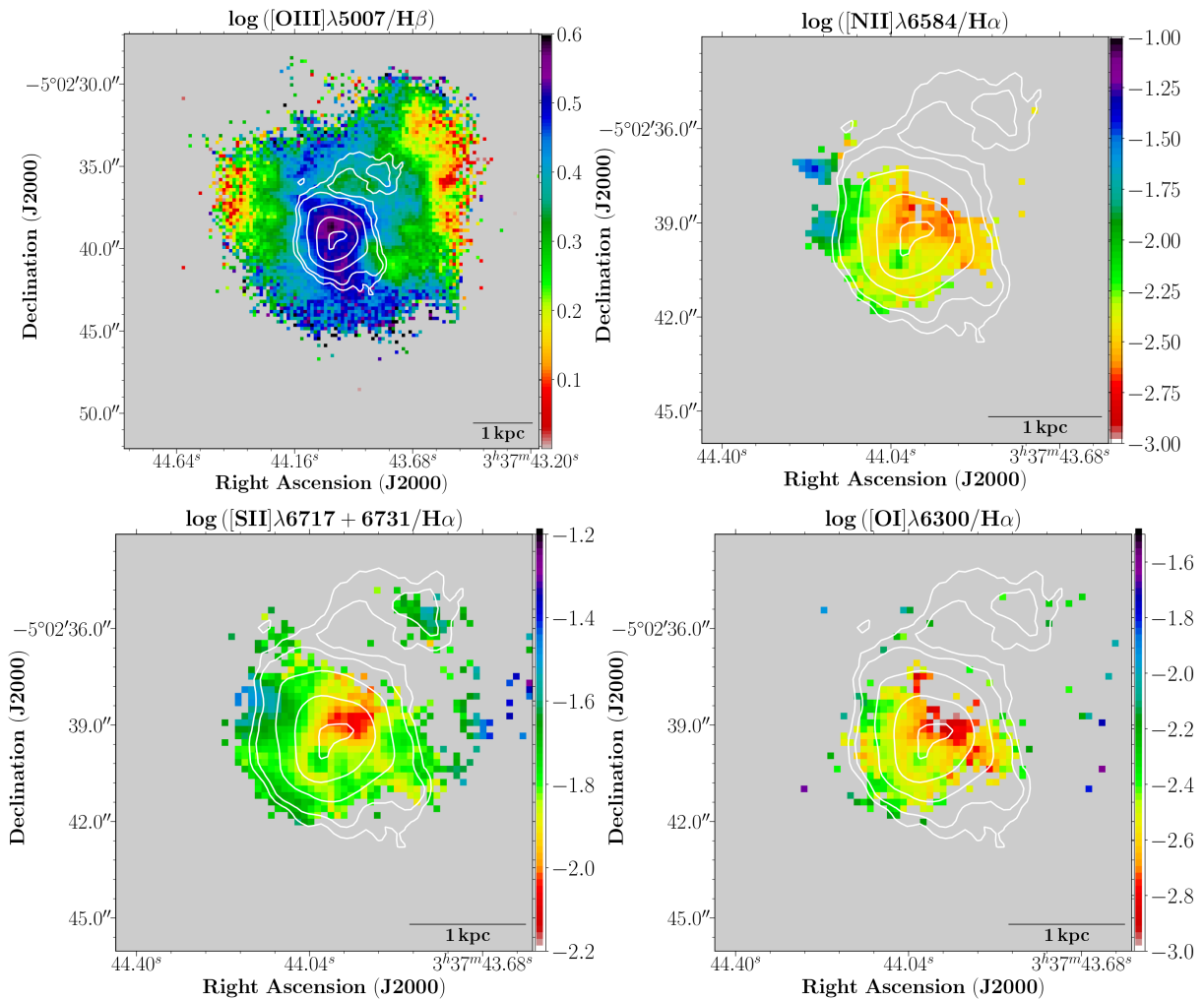


Figure 7. Line ratio maps of SBS 0335 – 052E: [O III] λ 5007/H β , [N II] λ 6584/H α , [S II] λ 6717,6731/H α , [O I] λ 6300/H α . Only line fluxes with S/N (per pixel) > 5 are plotted. All maps are presented in logarithmic scale. Isocontours of the He II λ 4686 emission line flux are shown overplotted for reference. East is to the left-hand side and North is up.

Thus, the role played by WRs in ionizing He⁺ at low metallicities is still uncertain.

The existence of a WR stellar population in SBS 0335 – 052E, despite its low Z , was first reported by Izotov et al. (1999). Later, Papaderos et al. (2006) and Izotov et al. (2006) showed the detection of WRs associated with SSC #3. We searched for WR features in all 0.2×0.2 arcsec² He II-emitting spaxels from MUSE. Our data set show indications of a WR bump centered at $\lambda \sim 4656$ Å in one spaxel nearby SSC #3, in agreement with Papaderos et al. (2006) and Izotov et al. (2006). In comparison with these works, the spatially resolved spectroscopy with high spatial resolution of MUSE allows us to give a more precise location of such WR feature which is found to be ~ 0.3 arcsec (~ 78 pc at the distance of SBS 0335 – 052E) southeast of SSC #3. Moreover, by adding the emission from three spaxels, we find a new WR detection, also at $\lambda \sim 4656$ Å. This new WR knot is located at ~ 1.4 arcsec (~ 360 pc at the distance of SBS 0335 – 052E) toward the west of the center of the SSCs complex⁵ (see Fig. 8).

⁵According to Eldridge, Langer & Tout (2011), for type Ib/c SN progenitors, 10 to 20 per cent of WRs could travel hundreds of pc from their birth places. This could be the case of the new WR knot detected here, but this discussion is beyond the framework of this paper.

The λ 4656 broad bump observed in the spectra of the two WR knots (see Fig. 8) can be read as a signature of early carbon WRs (WCE; e.g. Crowther & Hadfield 2006; Papaderos et al. 2006). In IZw18, a nearby galaxy with extremely low metallicity ($\sim 1/40$ solar metallicity; e.g. Vílchez & Iglesias-Páramo 1998; Kehrig et al. 2016), isolated clusters with WC stars have been detected as well (e.g. Brown et al. 2002). Detecting WRs in very metal-deficient objects is always an important observational constraint because it challenges current stellar evolutionary models for massive stars, which predict very few, if any, WRs in extremely metal-poor environments (e.g. Leitherer et al. 2014; Eldridge et al. 2017). Here, the total flux of the WCE bump measured from each WR knot spectrum provides a similar reddening-corrected luminosity of $L_{\text{WCE}} \sim 2.4 \times 10^{36}$ erg s⁻¹. Crowther & Hadfield (2006) computed WCE (WC4) models at the LMC and IZw18 metallicities, i.e. $12 + \log(\text{O}/\text{H}) \sim 8.36$ (e.g. Russell & Dopita 1990) and 7.11 (e.g. Kehrig et al. 2016), respectively.

As the metallicity of SBS 0335 – 052E [$12 + \log(\text{O}/\text{H}) \sim 7.3$] is closer to that of IZw18, we compared our observations with the IZw18-like WCE models to derive the number of WRs in SBS 0335 – 052E. Taking the luminosity of 3.5×10^{35} erg s⁻¹ for a single IZw18-like WC4 star (Crowther & Hadfield 2006),

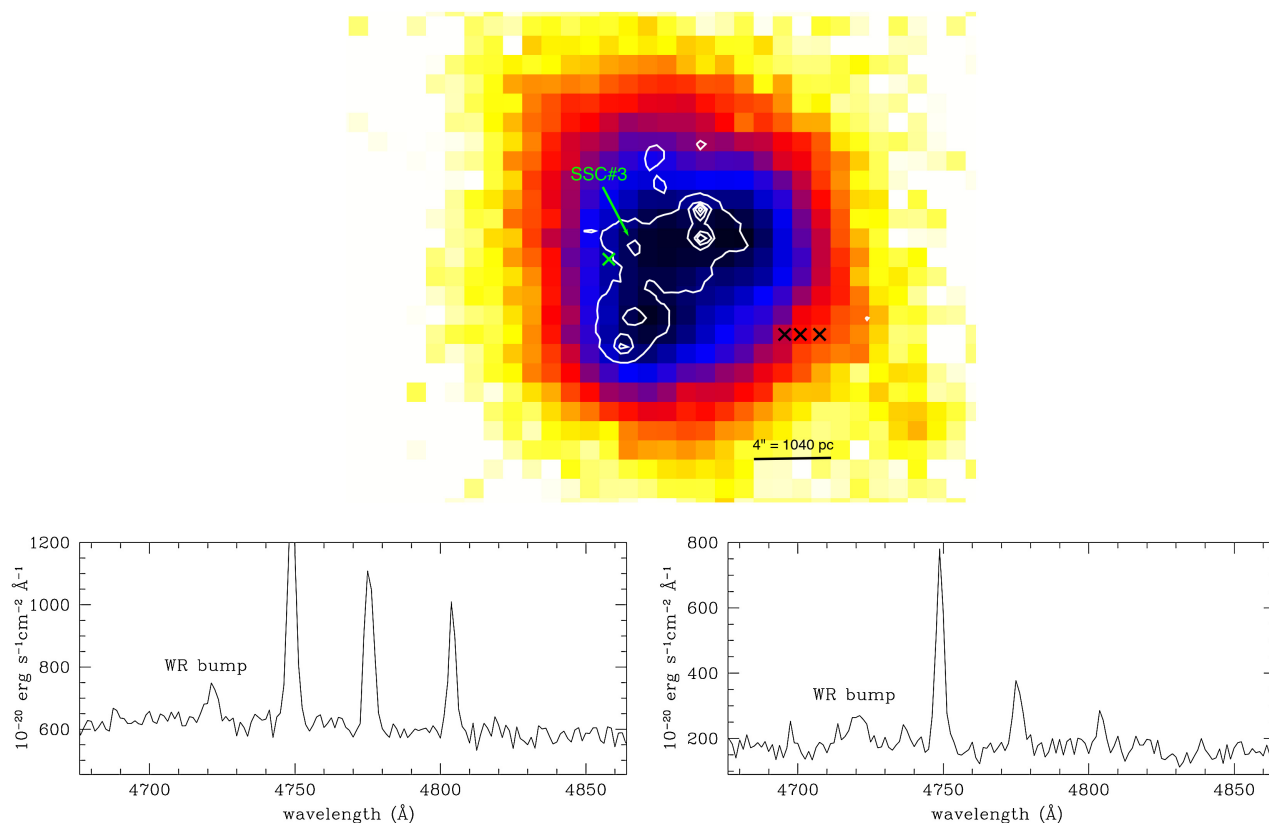


Figure 8. Top panel: Nebular He II $\lambda 4686$ map centered on the massive young SSCs whose positions are represented by the white contours. The crosses indicate the location of the WR knots detected in this work. Bottom row: spectra showing the WR bumps. Bottom left-hand panel: spectrum of the spaxel nearby SSC#3, indicated by the green cross in the top panel; Bottom righthand panel: spectrum obtained by adding the emission from the 3 spaxels marked with black crosses in the top panel.

this corresponds to an equivalent number of ~ 7 WCEs in each WR knot, i.e. a total of 14 WCEs in SBS 0335 – 052E. From these 14 WCEs, a total flux of $Q(\text{He II})=4.4 \times 10^{48}$ photon s^{-1} is expected (assuming $Q(\text{He II})=10^{47.5}$ photon s^{-1} for one IZw18-like WCE; Crowther & Hadfield 2006). This is about 500 times lower than the $Q(\text{He II})_{\text{He II-MB}}=2.25 \times 10^{51}$ for the He II main body region, and a factor of ~ 700 lower than the $Q(\text{He II})_{\text{int}}=3.17 \times 10^{51}$ derived from our data.

Based on the WCE models by Crowther & Hadfield (2006), therefore, more than 7000 WRs are required to explain the He II-ionization budget measured. Such a very large WR population is not supported by state-of-the-art stellar evolutionary models for (single and binary) massive stars in metal-poor environments (see e.g. Leitherer et al. 2014; Eldridge et al. 2017, and references therein), and it is not compatible with the total stellar mass of the six SSCs ($M_{*, \text{SSCs}} \sim 5.6 \times 10^6 M_{\odot}$; Reines et al. 2008) where the star formation in SBS 0335 – 052E is mostly concentrated; assuming a Salpeter initial mass function (IMF; Salpeter 1955) with $M_{\text{up}}=150 M_{\odot}$ ($M_{\text{up}}=300 M_{\odot}$), a cluster with > 7 (5) times the SSCs total mass would be needed to produce > 7000 WRs in SBS 0335 – 052E. Moreover, the nebular He II $\lambda 4686$ emission is by far more extended than the places occupied by the WR knots (see Fig. 8). Based on IFS studies, we have observed similar cases of spatial offset between WRs and He II $\lambda 4686$ -emitting regions for other nearby, metal-poor SF galaxies (see Kehrig et al. 2008, 2013, 2015). All this indicates that, although the contribution from WRs to He II-ionization cannot be disregarded, they are not exclusively responsible for the He II $\lambda 4686$ emission in SBS 0335 – 052E, in

line with other metal-deficient galaxies as mentioned above. The evolution of massive stars into WR stars is not well understood, and the number of WRs derived here is limited to the current available models for metal-poor WRs which suffer from still unresolved uncertainties (see e.g. Smith, Norris & Crowther 2002; Vink & de Koter 2005; Crowther & Hadfield 2006; Crowther 2007; Maeder & Meynet 2012).

Considering hot massive stars to be the primary source of He⁺-ionizing photons in SBS 0335 – 052E, as our IFS observations indicate, we need to investigate other types of stars besides WRs. Although classical nebulae ionized by O stars having $T_{\text{eff}} < 55\,000$ K are not expected to produce strong He⁺⁺, certain O stars are predicted to be hot enough to ionize He II (Kudritzki 2002). According to the hottest models ($T_{\text{e}}=60\,000$ K) of massive O stars at $Z \sim 3$ per cent (i.e. the SBS 0335 – 052E metallicity) by Kudritzki (2002), we infer that $\sim 16\,000$ stars with $150 M_{\odot}$ (with predicted $Q(\text{He II}) \approx 1.9 \times 10^{47}$ photon s^{-1} each; see fig.12 from Kudritzki 2002) are required to explain the derived $Q(\text{He II})_{\text{int}}$ budget. Alternatively, if we take the $300 M_{\odot}$ star hottest models (with $Q(\text{He II}) \approx 9 \times 10^{48}$ photon s^{-1} each), ~ 360 of these stars would be needed to produce the observed $Q(\text{He II})_{\text{int}}$. For a Salpeter IMF, 16 000 stars with $145 \leq M_{*}/M_{\odot} \leq 155$ would imply a cluster with $> 270 \times M_{*, \text{SSCs}}$; on the other hand, 360 stars with $290 \leq M_{*}/M_{\odot} \leq 310$ requires a cluster mass of $\sim 16 \times M_{*, \text{SSCs}}$. A Kroupa IMF (Kroupa 2001) does not solve the cluster mass issue neither.

Work in recent years has shown that rotation is a key ingredient in shaping the evolution of massive stars with very low metallicities ($Z < \text{SMC}$ metallicity down to Population III stars; see Meynet

& Maeder 2017, and references therein). Fast rotators (with initial $v_{rot} \gtrsim 300 \text{ km s}^{-1}$) are expected to lead to chemically homogeneous evolution (CHE) in which the star becomes brighter and hotter, and thus more ionizing photons, specially in the extreme UV, are emitted than in the corresponding non-rotating case (e.g. Brott et al. 2011; Levesque et al. 2012; Yoon, Dierks & Langer 2012). Presently, although we still know little about rotation velocities of massive stars and their variation with environment, observations seem to favor fast rotators at low Z (e.g. Martayan et al. 2007; Hunter et al. 2008). Model predictions suggest that the effects of rotation, like CHE, should be enhanced at lower metallicities. There is an increase of theoretical and observational evidence which supports the significant role of rotation among the generations of first stars, with $Z=0$ or extremely low metallicities, and fast rotating massive stars were likely common phenomena in the early Universe (e.g. Leitherer 2008; Chiappini et al. 2008; Maeder & Meynet 2012; Yoon et al. 2012). Modern models for low-metallicity massive fast-rotating single stars which undergo CHE have been published by Szécsi et al. (2015); the authors called them transparent wind UV intense stars (or TWUIN stars). Considering all this and the extremely low- Z of SBS 0335 – 052E, we compare our observations with the TWUINs predictions,⁶ following the same approach that we used previously for non-rotating WCE and massive O stellar models. Taking the computed $Q(\text{He II})=7.37 \times 10^{48} \text{ photon s}^{-1}$ for the most massive $294 M_{\odot}$ TWUIN, we require that ~ 430 (~ 300) such stars are necessary to explain the $Q(\text{He II})_{\text{Int}}$ ($Q(\text{He II})_{\text{He II-MB}}$). Again, hundreds of these super-massive TWUINs do not match the $M_{*,\text{SSCs}}$ of SBS 0335 – 052E. If we instead, apply the same approach using lower mass TWUIN models, it makes even harder to account for the observations. Besides the $Q(\text{He II})$ budget, we have measured values of $\text{He II } \lambda 4686/\text{H}\beta$ as high as 0.06 within the $\text{He II } \lambda 4686$ main body region. Under ionization-bounded conditions, even the most massive TWUIN models cannot reproduce these values of $\text{He II } \lambda 4686/\text{H}\beta$ (see table B.1 from Szécsi et al. 2015).

As mentioned in Section 1, searches for very metal-poor starbursts and PopIII-hosting galaxies at high- z using He II lines have been performed, and is among the main *JWST* science drivers (e.g. Schaerer 2008; Cassata et al. 2013; Visbal et al. 2015). This search is based on the predicted high effective temperature for PopIII stars which will emit a large number of photons with energy $> 54 \text{ eV}$, and also on the expected and observed increase of the nebular He II line with decreasing Z (e.g. Guseva et al. 2000; Schaerer 2003, 2008; Brinchmann et al. 2008). So a speculative possibility to explain the derived $Q(\text{He II})$ in SBS 0335 – 052E could be based on nearly metal-free ionizing stars. We have used recent models for fast-rotating $Z=0$ stars (Yoon et al. 2012) as an approximation for the He II ionizing output of nearly metal-free stars. According to these $Z=0$ models, we found that a significantly smaller number of such stars, in comparison with the models considered previously, could explain the observed He II budget; ~ 160 (230) stars with mass $M_{\text{ini}}=150 M_{\odot}$ (with $Q(\text{He II}) \approx 1.42 \times 10^{49} \text{ photon s}^{-1}$ each) would be sufficient to account for the $Q(\text{He II})_{\text{He II-MB}}$ ($Q(\text{He II})_{\text{Int}}$). Additionally, the ionizing spectra produced by these star models are hard enough to explain the highest $\text{He II } \lambda 4686/\text{H}\beta$ values observed, assuming that ionization-bounded conditions are met. Further speculation on the $Z=0$ stars hypothesis is beyond the scope of this paper.

⁶We note that the TWUIN models by Szécsi et al. (2015) are predicted at the IZw18 metallicity, i.e. slightly lower than the SBS 0335 – 052E metallicity.

Despite its nature as an entirely hypothetical scenario, it might suggest that stars with metallicity considerably lower than that of the He II regions in SBS 0335 – 052E are required to produce the total He II ionizing photon flux (see next Section).

5.3.2 Stellar Population Synthesis Models

The effects of stellar multiplicity have been recognized to play a key role when modelling young stellar populations (see Eldridge et al. 2017, and references therein). Recently, it has been suggested that most massive stars evolve as part of binary systems (e.g. Langer 2012; Sana et al. 2012, 2014). At low metallicities, different stellar evolution pathways, including those resulting from interacting binaries, are expected to become more and more important (e.g. Zhang et al. 2013; Stanway et al. 2014; Stanway, Eldridge & Becker 2016). According to population synthesis codes incorporating binary interactions, binarity leads to a bluer stellar population, and extends the lifetime of the WR stars up to ages later than 10 Myrs. This allows harder ionizing photons to exist at later times than expected from a single star population (e.g. Belkus et al. 2003; Zhang et al. 2015; Eldridge et al. 2017).

Here, we considered a suite of models from the most recent data release of *Binary Population and Spectral Synthesis* (BPASSv2.1; Eldridge et al. 2017). By integrating the predicted BPASS SEDs over the wavelength range $1 \text{ \AA} < \lambda < 228 \text{ \AA}$, we computed $Q(\text{He II})$ for all IMFs available on the BPASSv2.1 data release. For each IMF, we took into account the three lowest metallicity models: $Z=10^{-3}$, 10^{-4} , 10^{-5} . The models at $Z=10^{-3}$ correspond to the metallicity closest to that of SBS 0335 – 052E. A fundamental benefit of the new BPASSv2.1 is that now they have spectra at the lowest metallicities $Z=10^{-5}$ and 10^{-4} . We took advantage of this since the influence of massive stars on the synthetic spectrum is believed to be strongest at these low metallicities. Finally, for every set of models, we also considered the BPASS predictions which do not include binary evolution, i.e. the BPASS single-star models. Thus this set of models allows us to check the impact on the He II ionizing flux output by varying the IMF, metallicity and binarity. Our estimates assume an instantaneous burst at $10^{6.8} \text{ yr}$ because that model age matches the SSCs mean age of $\sim 6 \text{ Myr}$ (Thuan et al. 1997; Reines et al. 2008). The results obtained from the BPASSv2.1 models considered here are summarized in Table 2.

From Table 2, we see that, at a given IMF, the predicted $Q(\text{He II})$ always increases with decreasing metallicity, both for single-star and binary models. This effect is expected since stars at lower metallicity have hotter effective temperatures which boost the ionizing photon flux. We also found that the $Q(\text{He II})$ output of a binary population exceeds that of the single star population at all metallicities, regardless the IMF adopted. This outcome agrees with Eldridge et al. (2017) which predict a longer ionizing photon production lifetime of the binary stars overtaking the single stars at late ages for any ongoing or evolving starburst. Scaling the $Q(\text{He II})$ values from Table 2 to the $M_{*,\text{SSCs}}$ of $\sim 5.6 \times 10^6 M_{\odot}$, we infer that none of the models with $Z=10^{-3}$ (the Z that better match the SBS 0335 – 052E metallicity of $\sim 3\text{--}4$ per cent solar) can reproduce the observed integrated $Q(\text{He II})_{\text{Int}}=3.17 \times 10^{51} \text{ photon s}^{-1}$. At $Z=10^{-3}$, predicted $Q(\text{He II})$ reaches its maximum for the binary star model with IMF ‘imf100-300’; this value is $\sim 1.3 \times 10^{50} \text{ photon s}^{-1}$ ($= 2.39 \times 10^{49} \text{ photon s}^{-1}$ scaled to the $M_{*,\text{SSCs}}$; see Table 2), i.e. ~ 24 times lower than the derived $Q(\text{He II})_{\text{Int}}$.

The only two models that can explain the derived $Q(\text{He II})_{\text{Int}}$ budget are the binary ones at $Z=10^{-5}$ for a shallower

Table 2. Integrated Q(He II) from BPASSv2.1 for instantaneous starburst models of initial stellar mass $10^6 M_{\odot}$ at $10^{6.8}$ yr.

IMF ^a	Z (Z/Z _⊙) ^b	Q(He II) photon s ⁻¹	
		Single	Binary
imf100-100 ^c	10 ⁻⁵ (0.05 %)	1.40 × 10 ⁴⁹	7.89 × 10 ⁵⁰
	10 ⁻⁴ (0.5 %)	6.45 × 10 ⁴⁸	3.40 × 10 ⁵⁰
	0.001 (5 %)	5.05 × 10 ⁴⁶	2.18 × 10 ⁴⁹
imf100-300 ^c	10 ⁻⁵ (0.05 %)	1.20 × 10 ⁴⁹	7.37 × 10 ⁵⁰
	10 ⁻⁴ (0.5 %)	6.16 × 10 ⁴⁸	3.48 × 10 ⁵⁰
	0.001 (5 %)	4.30 × 10 ⁴⁶	2.39 × 10 ⁴⁹
imf135all-100 ^d	10 ⁻⁵ (0.05 %)	5.01 × 10 ⁴⁸	2.09 × 10 ⁵⁰
	10 ⁻⁴ (0.5 %)	2.29 × 10 ⁴⁸	8.97 × 10 ⁴⁹
	0.001 (5 %)	1.77 × 10 ⁴⁶	5.94 × 10 ⁴⁸
imf135-100 ^e	10 ⁻⁵ (0.05 %)	6.87 × 10 ⁴⁸	2.71 × 10 ⁵⁰
	10 ⁻⁴ (0.5 %)	3.10 × 10 ⁴⁸	1.16 × 10 ⁵⁰
	0.001 (5 %)	2.40 × 10 ⁴⁶	7.68 × 10 ⁴⁸
imf135-300 ^e	10 ⁻⁵ (0.05 %)	6.59 × 10 ⁴⁸	2.79 × 10 ⁵⁰
	10 ⁻⁴ (0.5 %)	2.98 × 10 ⁴⁸	1.27 × 10 ⁵⁰
	0.001 (5 %)	2.30 × 10 ⁴⁶	8.99 × 10 ⁴⁸
imf170-100 ^f	10 ⁻⁵ (0.05 %)	2.60 × 10 ⁴⁸	7.22 × 10 ⁴⁹
	10 ⁻⁴ (0.5 %)	1.16 × 10 ⁴⁸	3.07 × 10 ⁴⁹
	0.001 (5 %)	8.77 × 10 ⁴⁵	2.13 × 10 ⁴⁸
imf170-300 ^f	10 ⁻⁵ (0.05 %)	2.58 × 10 ⁴⁸	7.62 × 10 ⁴⁹
	10 ⁻⁴ (0.5 %)	1.15 × 10 ⁴⁸	3.43 × 10 ⁴⁹
	0.001 (5 %)	8.70 × 10 ⁴⁵	2.46 × 10 ⁴⁸

Notes. ^aIMFs are labelled following the BPASSv2.1 designation (Eldridge et al. 2017).

^bBPASS models assume Z_⊙=0.02 for consistency with their empirical mass-loss rates which were scaled from this value.

^cimf100-100: $\alpha_1 = -1.30$ (0.1–0.5 M_⊙), $\alpha_2 = -2.00$ (0.5–100 M_⊙); imf100-300: as imf100-100 but with M_{up}=300 M_⊙.

^dSalpeter IMF with M_{up}=100 M_⊙.

^eThese are the default IMFs recommended by Eldridge et al. (2017); imf135-100: $\alpha_1 = -1.30$ (0.1–0.5 M_⊙), $\alpha_2 = -2.35$ (0.5–100 M_⊙); imf135-300: as imf135-100 but with M_{up}=300 M_⊙.

^fimf170-100: $\alpha_1 = -1.30$ (0.1–0.5 M_⊙), $\alpha_2 = -2.70$ (0.5–100 M_⊙); imf170-300: as imf170-100 but with M_{up}=300 M_⊙.

‘top-heavy’ IMF with either M_{up}=100 M_⊙ (‘imf100-100’) or M_{up}=300 M_⊙ (‘imf100-300’); both predict a similar Q(He II) of $\sim 4.4 \times 10^{51}$ photon s⁻¹ or 4.1×10^{51} photon s⁻¹ (after scaling to the M_{*},_{SSCs}; see Table 2), respectively. These predictions exceed the observed Q(He II)_{int} which could suggest that some fraction of the He⁺-ionizing photons may be able to escape the galaxy. Previous work claim that up to ~ 50 per cent of the hydrogen ionizing flux could be leaking out the H II regions of SBS 0335 – 052E, possibly due to clumping and filaments in its ISM (see e.g. Reines et al. 2008; Johnson et al. 2009; Herenz et al. 2017). These structures in the ionized gas might be acting as escape pipes for the He II Lyman continuum as well.

Thus, the outcomes from the BPASSv2.1 code indicate that while calling upon super-massive stars (M > 100 M_⊙) is not essential, a binary population distributed over a ‘top-heavy’ IMF seem to be required to clear up the observed He II flux budget. More interestingly, according to these modern models, stars with metallicity (Z=0.05 per cent solar) much lower than that of the ionized gas (Z ~ 3 –4 per cent solar) of SBS 0335 – 052E are to be invoked to explain the He II ionization in this galaxy. We highlight that similar results have been found to account for by the He II ionization in other nearby, metal-poor SF galaxies (see Kehrig et al. 2015; Senchyna et al. 2017). Certainly, in this hypothetical scenario, such very metal-poor stars cannot belong to the same SSCs which host more chemically evolved objects. Further investigation is needed to understand the origin of this apparent inconsistency. Nevertheless, we should bear in mind the uncertainties yet unsolved in the BPASS code; the reader is referred to Section 7 from Eldridge et al. (2017) for details. Also, caution should be exercised when evaluating the Z=10⁻⁵ and 10⁻⁴ models; empirical data for stellar atmospheres

at these low Z are not available, and thus consist of theoretical extrapolation from higher-Z atmospheres which are better tested.

Although a detailed comparison between atmosphere and wind models is beyond the scope of this work, intermediate-mass stripped stars could be an important source of hard ionizing radiation. Such stars, thought to be very hot objects emitting the majority of their photons in the extreme UV, have been stripped of their envelope through interaction with a binary companion (Götberg, de Mink & Groh 2017). Götberg et al. (2018) computed atmosphere models for these stars, but they are not yet considered in BPASS, and thus we have not considered them here. Although models suggest that their importance decreases with decreasing metallicity and thus should not be relevant for extremely metal-poor objects, the Q(He II) photon flux predictions of such stars are still uncertain (Götberg et al. 2018), and any conclusion about their role in galaxies like SBS0335 – 052 would be premature.

6 SUMMARY AND CONCLUDING REMARKS

Observational data of high-ionization lines, like He II, in the reionization era have been recently accumulated, and there is a growing body of evidence that He II-emitters are more frequent among high-z galaxies. Narrow He II emission has been claimed to be a good tracer of the elusive PopIII-stars. The He II line is in comfortable reach of next generation telescopes, like JWST and ELT, which will detect the rest-frame UV of thousands of galaxies during the epoch of reionization. In light of these new and upcoming observations, a more sophisticated understanding of the high-ionization phenomenon at $z \sim 0$ is pivotal to interpret the data in a physically meaningful manner, and to possibly constrain sources responsible for the H and He II

reionization epochs. Optical MUSE-Integral Field Unit (IFU) and X-ray *Chandra* observations of the nearby, extremely metal-poor bursty-galaxy SBS 0335 – 052E with nebular He II emission are presented in this work. Such objects are excellent primordial analogues that can provide clues to the physical properties of galaxies in the early Universe.

Based on the MUSE data, we created spectral maps of relevant emission lines in the optical range. These data provide us with a new 2D view of the ionized ISM in SBS 0335 – 052E, in particular, the high-ionization nebular He II $\lambda 4686$ line (see also Herenz et al. 2017). We find a highly extended He II $\lambda 4686$ -emitting region reaching distances $\gtrsim 1.5$ Kpc from the youngest SSCs. The He II $\lambda 4686$ map shows three maxima which are offset from the brightest UV SSCs. We took benefit of our IFU data to create 1D spectra of several regions based on the spatial distribution of the He II $\lambda 4686$ emission. For the first time, using the derived SBS 0335 – 052E integrated spectrum, we recovered the entire nebular He II emission and compute the corresponding total He II-ionization budget, $Q(\text{He II})_{\text{int}} \approx 3.17 \times 10^{51}$ photon s^{-1} . As we showed in Kehrig et al. (2015), this observational quantity is essential to perform a free-aperture investigation on the formation of narrow He II line.

From our analysis of the combined MUSE and *Chandra* data, we infer that the $Q(\text{He II})$ provided by the X-ray emission from SBS 0335 – 052E is well below the needed value to ionize He⁺ at the level measured in this galaxy. Although we cannot discard some contribution to the He II excitation from shocks, our spaxel-by-spaxel study from MUSE favors hot massive stars as the main agent of the He II ionization in SBS 0335 – 052E.

Using the MUSE observations we located two WR knots from which one is identified for the first time here. The WR knot spectra reveal the presence of carbon-type WR stars in SBS 0335 – 052E. In comparison with long-slit or single-fiber spectroscopy, the IFS technique can enhance the contrast of the WR bump emission against the galaxy continuum. This minimizes the WR bump dilution, also allowing the identification of WR stars where they were not detected before (see also Kehrig et al. 2008, 2013). To investigate the stellar source scenario, we compare observations with stellar models applying two approaches; a more simple one which makes use of models of (rotating and non-rotating) single massive stars on a star-by-star basis, and a second one based on the new release of stellar population synthesis BPASSv2.1. We demonstrated that both approaches have merits, and taken together, they can provide guidance to interpret the observations. The star-by-star study points out that WRs solely cannot explain the He II-ionizing energy budget derived for SBS 0335 – 052E. From the BPASSv2.1 code, we show that only the binary models with a ‘top-heavy’ IMF (i.e. non-standard IMF) at $Z=10^{-5}$ (i.e. $Z \sim 70$ times lower than the Z of the ionized gas in SBS 0335 – 052E) provide sufficient He⁺-ionizing photons to explain the observed $Q(\text{He II})_{\text{int}}$. The approach on a star-by-star basis also suggests that stars more metal-deficient than the galaxy main body are required. Investigating such metallicity discrepancy at $z \sim 0$ feels the necessity for additional research, and it is fundamental to interpret high-ionization emission in the distant Universe.

This paper shows the need to identify nearby, metal-poor He II-emitters, like SBS 0335 – 052E. IFS studies of such galaxies enable extended insight into their ‘realistic’ ISM and massive stars, therefore providing constraints on high-redshift galaxy evolution, and on metal-poor stellar models. This work can guide through the preparation of forthcoming searches for primeval objects, one of the main science drivers for next-generation telescopes.

ACKNOWLEDGEMENTS

This study is based on observations collected at the European Southern Observatory. We are very grateful to our referee for providing constructive comments and help in improving the manuscript. This work has been partially funded by research project AYA2017-79724-C4-4-P from the Spanish PNYA. CK, JMV, SDP, and JI-P acknowledge financial support from Junta de Andalucía Excellence Project PEX2011-FQM705. MAG acknowledges support of the grant AYA 2014-57280-P, co-funded with FEDER funds. LKH thanks the Instituto de Astrofísica de Andalucía-CSIC for warm hospitality in the visit during which the work for this paper was initiated. This work made use of the v2.1 of the Binary Population and Spectral Synthesis (BPASS) models as last described in Eldridge et al. (2017).

REFERENCES

- Allen M. G., Groves B. A., Dopita M. A., Sutherland R. S., Kewley L. J., 2008, *ApJS*, 178, 20
- Arnaud K. A., 1996, *ASPC*, 101, 17
- Asplund M., Grevesse N., Sauval A. J., Scott P., 2009, *ARA&A*, 47, 481
- Bacon R. et al., 2014, *The Messenger*, 157, 13
- Baldwin J. A., Phillips M. M., Terlevich R., 1981, *PASP*, 93, 5
- Belkus H., Van Bever J., Vanbeveren D., van Rensbergen W., 2003, *A&A*, 400, 429
- Berg D. A., Erb D. K., Auger M. W., Pettini M., Brammer G. B., 2018, *ApJ*, 859, 164
- Blair W. P., Kirshner R. P., Chevalier R. A., 1981, *ApJ*, 247, 879
- Bouwens R. J., Illingworth G. D., Oesch P. A., Caruana J., Holwerda B., Smit R., Wilkins S., 2015, *ApJ*, 811, 140
- Brinchmann J., Kunth D., Durret F., 2008, *A&A*, 485, 657
- Bromm V., 2013, *RPPH*, 76, 112901
- Brott I. et al., 2011, *A&A*, 530, A115
- Brown T. M., Heap S. R., Hubeny I., Lanz T., Lindler D., 2002, *ApJ*, 579, L75
- Cardelli J. A., Clayton G. C., Mathis J. S., 1989, *ApJ*, 345, 245
- Cassata P. et al., 2013, *A&A*, 556, A68
- Cerviño M., Mas-Hesse J. M., Kunth D., 2002, *A&A*, 392, 19
- Chiappini C., Ekström S., Meynet G., Hirschi R., Maeder A., Charbonnel C., 2008, *A&A*, 479, L9
- Crowther P. A., 2007, *ARA&A*, 45, 177
- Crowther P. A., Hadfield L. J., 2006, *A&A*, 449, 711
- Davies R. L. et al., 2017, *MNRAS*, 470, 4974
- Dijkstra M., Mesinger A., Wyithe J. S. B., 2011, *MNRAS*, 414, 2139
- Dopita M. A., Sutherland R. S., 1996, *ApJS*, 102, 161
- Eldridge J. J., Langer N., Tout C. A., 2011, *MNRAS*, 414, 3501
- Eldridge J. J., Stanway E. R., Xiao L., McClelland L. A. S., Taylor G., Ng M., Greis S. M. L., Bray J. C., 2017, *PASA*, 34, e058
- Fialkov A., Barkana R., Visbal E., 2014, *Nature*, 506, 197
- García M., Herrero A., Najarro F., Lennon D. J., Alejandro Urbaneja M., 2014, *ApJ*, 788, 64
- Garnett D. R., Kennicutt R. C., Jr, Chu Y.-H., Skillman E. D., 1991, *ApJ*, 373, 458
- Georgy C., Hirschi R., Ekström S., 2017, in Zwintz K., Poretti E., eds, *Proceedings of the Polish Astronomical Society, Vol. 5, Second BRIT-Constellation Science Conference: Small satellites—big science*. Polish Astronomical Society, Poland, p. 37
- Gomes J. M. et al., 2016, *A&A*, 588, A68
- Götberg Y., de Mink S. E., Groh J. H., 2017, *A&A*, 608, A11
- Götberg Y., de Mink S. E., Groh J. H., Kupfer T., Crowther P. A., Zapartas E., Renzo M., 2018, *A&A*, 615, A78
- Gräfener G., Vink J. S., 2015, *A&A*, 578, L2
- Guseva N. G., Izotov Y. I., Thuan T. X., 2000, *ApJ*, 531, 776
- Hadfield L. J., Crowther P. A., 2007, *MNRAS*, 381, 418

- Herenz E. C., Hayes M., Papaderos P., Cannon J. M., Bik A., Melinder J., Östlin G., 2017, *A&A*, 606, L11
- Herrero A., Garcia M., Puls J., Uytterhoeven K., Najarro F., Lennon D. J., Rivero-González J. G., 2012, *A&A*, 543, A85
- Hunter I., Lennon D. J., Dufton P. L., Trundle C., Simón-Díaz S., Smartt S. J., Ryans R. S. I., Evans C. J., 2008, *A&A*, 479, 541
- Izotov I. I., Guseva N. G., Lipovetskiĭ V. A., Kniazev A. I., Stepanian J. A., 1990, *Nature*, 343, 238
- Izotov Y. I., Lipovetsky V. A., Chaffee F. H., Foltz C. B., Guseva N. G., Kniazev A. Y., 1997, *ApJ*, 476, 698
- Izotov Y. I., Chaffee F. H., Foltz C. B., Green R. F., Guseva N. G., Thuan T. X., 1999, *ApJ*, 527, 757
- Izotov Y. I., Schaerer D., Blecha A., Royer F., Guseva N. G., North P., 2006, *A&A*, 459, 71
- Johnson K. E., Hunt L. K., Reines A. E., 2009, *AJ*, 137, 3788
- Kauffmann G. et al., 2003, *MNRAS*, 346, 1055
- Kehrig C., Vílchez J. M., Sánchez S. F., Telles E., Pérez-Montero E., Martín-Gordón D., 2008, *A&A*, 477, 813
- Kehrig C. et al., 2011, *A&A*, 526, A128
- Kehrig C. et al., 2012, *A&A*, 540, A11
- Kehrig C. et al., 2013, *MNRAS*, 432, 2731
- Kehrig C., Vílchez J. M., Pérez-Montero E., Iglesias-Páramo J., Brinchmann J., Kunth D., Durret F., Bayo F. M., 2015, *ApJ*, 801, L28
- Kehrig C. et al., 2016, *MNRAS*, 459, 2992
- Kewley L. J., Dopita M. A., Sutherland R. S., Heisler C. A., Trevena J., 2001, *ApJ*, 556, 121
- Kewley L. J., Groves B., Kauffmann G., Heckman T., 2006, *MNRAS*, 372, 961
- Kewley L. J., Zahid H. J., Geller M. J., Dopita M. A., Hwang H. S., Fabricant D., 2015, *ApJ*, 812, L20
- Kroupa P., 2001, *MNRAS*, 322, 231
- Kudritzki R. P., 2002, *ApJ*, 577, 389
- Langer N., 2012, *ARA&A*, 50, 107
- Leitherer C., 2008, *Proc. IAU Symp. 255, Revision of Star-Formation Measures*. Kluwer, Dordrecht, p. 305
- Leitherer C., Ekström S., Meynet G., Schaerer D., Agienko K. B., Levesque E. M., 2014, *ApJS*, 212, 14
- Levesque E. M., Leitherer C., Ekstrom S., Meynet G., Schaerer D., 2012, *ApJ*, 751, 67
- Maeder A., Meynet G., 2012, *Rev. Mod. Phys.*, 84, 25
- Mainali R., Kollmeier J. A., Stark D. P., Simcoe R. A., Walth G., Newman A. B., Miller D. R., 2017, *ApJ*, 836, L14
- Markwardt C. B., 2009, in Bohlender D. A., Durand D., Dowler P., eds, *ASP Conf. Ser. Vol. 411, Astronomical Data Analysis Software and Systems XVIII*. Astron. Soc. Pac., San Francisco, p. 251
- Martayan C., Frémat Y., Hubert A.-M., Floquet M., Zorec J., Neiner C., 2007, *A&A*, 462, 683
- Massey P., 2013, *NewAR*, 57, 14
- Massey P., Neugent K. F., Morrell N., Hillier D. J., 2014, *ApJ*, 788, 83
- Melnick J., Heydari-Malayeri M., Leisy P., 1992, *A&A*, 253, 16
- Meynet G., Maeder A., 2017, in Alsabti A., Murdin P., eds, *Supernovae from Rotating Stars. Handbook of Supernovae*. Springer International Publishing, Switzerland, AG, p. 601
- Muijres L., Vink J. S., de Koter A., Hirschi R., Langer N., Yoon S.-C., 2012, *A&A*, 546, A42
- Neugent K. F., Massey P., 2011, *ApJ*, 733, 123
- Osterbrock D. E., Ferland G. J., 2006, *Astrophysics of Gaseous Nebulae and Active Galactic Nuclei*, 2nd. ed. University Science Books, Sausalito, CA
- Papaderos P., Izotov Y. I., Guseva N. G., Thuan T. X., Fricke K. J., 2006, *A&A*, 454, 119
- Puls J., Vink J. S., Najarro F., 2008, *A&AR*, 16, 209
- Reines A. E., Johnson K. E., Hunt L. K., 2008, *AJ*, 136, 1415
- Russell S. C., Dopita M. A., 1990, *ApJS*, 74, 93
- Salpeter E. E., 1955, *ApJ*, 121, 161
- Sana H. et al., 2012, *Sci*, 337, 444
- Sana H. et al., 2014, *ApJS*, 215, 15
- Sander A. A. C., Hamann W.-R., Todt H., Hainich R., Shenar T., 2017, *A&A*, 603, A86
- Schaerer D., 1996, *ApJ*, 467, L17
- Schaerer D., 2003, *A&A*, 397, 527
- Schaerer D., 2008, *Proc. IAU Symp. 255, Searching for Pop III Stars and Galaxies at High Redshift*. Kluwer, Dordrecht, p. 66
- Schaerer D., Vacca W. D., 1998, *ApJ*, 497, 618
- Senchyna P. et al., 2017, *MNRAS*, 472, 2608
- Shirazi M., Brinchmann J., 2012, *MNRAS*, 421, 1043
- Skillman E. D., 1985, *ApJ*, 290, 449
- Smith N., 2014, *ARA&A*, 52, 487
- Smith R. C., Kirshner R. P., Blair W. P., Long K. S., Winkler P. F., 1993, *ApJ*, 407, 564
- Smith L. J., Norris R. P. F., Crowther P. A., 2002, *MNRAS*, 337, 1309
- Stanway E. R., Eldridge J. J., Becker G. D., 2016, *MNRAS*, 456, 485
- Stanway E. R., Eldridge J. J., Greis S. M. L., Davies L. J. M., Wilkins S. M., Bremer M. N., 2014, *MNRAS*, 444, 3466
- Stark D. P., 2016, *ARA&A*, 54, 761
- Szécsi D., Langer N., Yoon S.-C., Sanyal D., de Mink S., Evans C. J., Dermine T., 2015, *A&A*, 581, A15
- Thuan T. X., Izotov Y. I., 2005, *ApJS*, 161, 240
- Thuan T. X., Izotov Y. I., Lipovetsky V. A., 1997, *ApJ*, 477, 661
- Thuan T. X., Bauer F. E., Papaderos P., Izotov Y. I., 2004, *ApJ*, 606, 213
- Tramper F., Sana H., de Koter A., Kaper L., 2011, *ApJ*, 741, L8
- Tumlinson J., Shull J. M., 2000, *ApJ*, 528, L65
- Veilleux S., Osterbrock D. E., 1987, *ApJS*, 63, 295
- Vílchez J. M., Iglesias-Páramo J., 1998, *ApJ*, 508, 248
- Vink J. S., de Koter A., 2005, *A&A*, 442, 587
- Visbal E., Haiman Z., Bryan G. L., 2015, *MNRAS*, 450, 2506
- Visbal E., Haiman Z., Bryan G. L., 2016, *MNRAS*, 460, L59
- Visbal E., Bryan G. L., Haiman Z., 2017, *MNRAS*, 469, 1456
- Windhorst R. A., Cohen S. H., Jansen R. A., Conselice C., Yan H., 2006, *New Astron. Rev.*, 50, 113
- Yoon S.-C., Dierks A., Langer N., 2012, *A&A*, 542, A113
- Zhang Y., Liu J., Zhang F., Han Z., 2013, *A&A*, 554, A136
- Zhang F., Li L., Cheng L., Wang L., Kang X., Zhuang Y., Han Z., 2015, *MNRAS*, 447, L21

This paper has been typeset from a $\text{\TeX}/\text{\LaTeX}$ file prepared by the author.